Revisiting the cubic crystal structures of $Sr_4Nb_2O_9$ and $Sr_5Nb_2O_{10}$

Jing-Yi Li[1,4], Chun-Hai Wang[1, 2,*], Xiao-Ming Wang[3], Chris D Ling[2], Brendan J Kennedy[2,*]

[1] State Key Laboratory of Solidification Processing, Northwestern Polytechnical University, Xi'an, Shaanxi 710072, China

[2] School of Chemistry, The University of Sydney, Sydney NSW 2006, Australia

[3] School of Chemistry & Chemical Engineering, Shaanxi Normal University, Xi'an, Shaanxi, 710062, China

[4]Department of Materials, University of Manchester, M13 9PL, UK.

Abstract

We have synthesized polycrystalline and single crystal samples of $Sr_4Nb_2O_9$ and $Sr_5Nb_2O_{10}$ and revisited the crystal structure of the high-temperature cubic phase. By careful analysis of single-crystal X-ray diffraction (SXRD), powder synchrotron X-ray diffraction (Syn-PXRD) and powder neutron diffraction (PND) data, we arrive at a structure model in space group $F\bar{4}3m$ (216), a subgroup of the reported $Fm\bar{3}m$ (225) model. The $F\bar{4}3m$ model gives a better fit to the diffraction data, especially PND. We observed an interstitial oxide ion O3 on the 48*h* site near O1, which gives a tetrahedral Nb1−O polyhedron rather than an octahedral one as found in the $Fm\bar{3}m$ (225) model. The temperature-dependent conductivities of $Sr_4Nb_2O_9$ and $Sr_5Nb_2O_{10}$ in dried O_2 were studied using impedance spectroscopy. The activation energies of $Sr_4Nb_2O_9$ and $Sr_5Nb_2O_{10}$ were estimated to be 1.18(1) eV and 1.17(4) eV respectively. This crystallographic arrangement of O1 and O3 (spread over split sites) is likely a key structural factor behind oxide ionic migration in $Sr_4Nb_2O_9$ and $Sr_5Nb_2O_{10}$.

Introduction

Solid oxide fuel cells (SOFCs) are an electrochemical approach to energy storage and production, delivering high electrical efficiency and significant environmental benefits especially due to their potential for high efficiency (>70% with fuel regeneration). SOFCs produces electricity by the oxidation of a fuel by oxygen ions that diffuse through an ionic conductor electrolyte layer[1]. From the investigations reported to date, the main limitation of SOFCs is the high activation temperatures of the commonly employed electrolytes (i.e., oxide ionic conductors). Therefore, considerable effort has been directed towards the search for low-temperature oxide ionic

* Corresponding Author, email: chwang81@gmail.com

conductors. An ideal oxygen ionic conductor is expected to give a $\geq 10^{-1}$ S/cm oxide ionic conductivity (and low electronic conductivity) at temperatures not appreciably above ambient [2, 3]. The most widely studied oxide ionic conductor is yttria-stabilized zirconia (YSZ), for which ionic conductivity of 0.1 S/cm at 1000 ºC has been observed in 8 mol% Y_2O_3-ZrO_2 (8YSZ)[4]. Promising results have been observed in other systems, such as CeO_2, Bi_2O_3 based oxides, $LaGaO_3$ based perovskites, $Bi_4V_2O_{11}$ and $La_2Mo_2O_9$ based derivatives, $Ba_2In_2O_5$ derivatives, brownmillerite like phases and pyrochlores[1, 2, 4, 5]. These, like YSZ, require high operating temperatures, generally above 600 ºC or even 750 ºC, leading to many engineering problems in the realms of efficiency, safety, thermal expansion matching of components, and sealants. Increased utilisation of SOFCs therefore depend on lowering the operation temperature through the development of new oxide ionic conductors.

Oxygen-deficient (oxygen vacancy or interstitial) perovskite materials often show high ionic conductivities. The complex perovskite $Sr_{4+x}Nb_2O_{9+x}$ (x = 0−2) system has been reported to exhibit good oxide ionic and protonic conductivities. The solid-solutions $Sr_{4+x}Nb_2O_{9+x}$ were proposed by Grivel & Li and by Chan *et al*. [6, 7] The parent $Sr_4Nb_2O_9$ can be considered as a complex perovskite with ideal atomic ratios $Sr(Sr_{1/3}Nb_{2/3})O_3$ across the solid-solution. Based on electron diffraction measurements of samples prepared at different temperatures, Levin *et al*. [8] suggested that $Sr_4Nb_2O_9$ forms a cubic high-temperature phase at $T \geq 1200$ ºC that transforms to a monoclinic phase ($P2_1/n$, 14) at $T < 1200$ ºC and a phase mixture (incommensurate, pseudotetragonal, monoclinic, and pseudocubic with different Sr−Nb orderings) at $T \leq 900$ ºC. They found that the phase transition temperature is quite slow (≥72 h). However, they did not give more structural details of the low-temperature phases except for a possible unit cell.

Li and Hong recently studied the high-temperature phase of $Sr_{4+x}Nb_2O_{9+x}$ using samples synthesized at 1250 ºC (1523 K) by combined Rietveld-refinement against powder X-ray and neutron diffraction data[6]. They found a 1:1 cation-ordered rock-salt type complex perovskite structure in space group $Fm\bar{3}m$(225) with the general formula $Sr_4(Sr_{2-2x}Nb_{2+2x})O_{11+3x}$ or $Sr_{6-2x}Nb_{2+2x}O_{11+3x}$ (x = 0.103−0.333)[6]. There are two cation sites, 8*c* (0.25 0.25 0.25) and 4*a* (0 0 0), occupied by Sr^{2+} and Nb^{5+} ions respectively; and one cation site, 4*b* (0.5 0.5 0.5), randomly co-occupied by the remaining Sr^{2+} and Nb^{5+}. For the anion sites, besides the ideal 24*e* (x_1 0 0) site in the complex perovskite structure, an interstitial site 48*h* (0, y_2, y_2) was also observed. Recently, we collected synchrotron X-ray and neutron diffraction data for cubic $Sr_4Nb_2O_9$ and $Sr_5Nb_2O_{10}$ (x = 1/3 and 1/7 in $Sr_{6-2x}Nb_{2+2x}O_{11+3x}$) samples. We found that the reported $Fm\bar{3}m$ model did not provide an ideal fit, and that a better model is therefore needed.

In the present work, we investigated the cubic phase of $Sr_4Nb_2O_7$ and $Sr_5Nb_2O_{10}$ and reported a new structure

model based on the high-resolution synchrotron X-ray and neutron powder diffraction and laboratory X-ray single crystal diffraction analysis. We also investigated the ionic conductivity of both samples by impedance measurements.

Experimental section

Sample Synthesis. Polycrystalline samples of $Sr_4Nb_2O_9$ and $Sr_5Nb_2O_{10}$ were synthesized by solid-state reaction. Stoichiometric amounts of 400 ℃ dried Nb_2O_5 and $SrCO_3$ (both Aldrich, >99.9%) were weighed and ground in an agate mortar and pestle. The well-mixed powders were placed into an open alumina crucible and calcined at different temperatures with several intermediate regrinding. Samples for powder diffraction measurements were calcined at 1350 ℃ for a total of 96 h and then air-quenched to room temperature to control the crystallization for high profile-quality. Sample for ceramic sintering (pellets for impedance measurements or rods for single crystal growth) were calcined at 1150 ℃ for a total of 96 h to achieve an ideal ceramic sintering activity.

To make ceramic pellets, the calcined powder was uniaxially pressed into pellets in a steel die with 5% polyvinyl alcohol (PVA) solution as the binder. The pellets were then calcined at 500 ℃ for 1 h to remove PVA, and sintered at 1450 °C for 6 h with a ramp of 5 °C/min. Finally, the pellets were cooled to 500 ℃ with a rate of 5 °C/min and naturally cooled in the furnace. To make ceramic rods, the calcined powder was pressed into rods at 40 MPa using a hydrostatic press and sintered 1450 °C for 6 h with a ramp of 5 °C/min.

Single crystals of $Sr_4Nb_2O_7$ and $Sr_5Nb_2O_{10}$ were grown using an optical floating zone furnace (FZF) equipped with four 300 W halogen lamps. The sintered sample rods were mounted inside a quartz tube of the furnace with 200 sccm (standard cubic centimeter per minute) argon and 50 sccm oxygen gas flowing to simulate air. The feed and seed rods were counter-rotated at 20 rpm throughout the experiment. Growth was carried out at a rate of 2 mm/h and was terminated after ~15 mm. The as-grown cylindrical-like crystal boule was light brown.

Powder Diffraction. Powder neutron diffraction (PND) data of $Sr_4Nb_2O_9$ and $Sr_5Nb_2O_{10}$ were collected on the high-resolution powder diffractometer ECHIDNA[9] at the OPAL research reactor, ANSTO, Australia. Around 10 g powder sample was loaded into an 8 mm diameter vanadium can. The PND data were collected at room temperature using neutrons of wavelength $\lambda = 2.4395$ Å over a 6.5−164° 2θ range (corresponding to a d-spacing range 21.515−1.2317 Å).

Synchrotron X-ray powder diffraction data (Syn-PXRD) were collected on the Powder Diffraction beamline at the Australian Synchrotron[10]. The well-ground $Sr_4Nb_2O_9$ and $Sr_5Nb_2O_{10}$ powders were loaded into 0.2 mm diameter capillaries and sealed before data collection. The data (Debye-Scherrer method) were collected using an array of Mythen microstrip detectors at room temperature from 0.5−80° 2θ with X-rays of wavelength λ =

0.774347 Å, which covers the d-spacing range 88.73391−0.602335 Å. To account for a gap between two individual detector modules, two sets of data were collected to improve the data accuracy with the detector offset was set at 0.5°, which were merged to a single data set by using the PDViPeR software.

Single crystal diffraction. Samples for single crystal X-ray diffraction (SXRD) measurements were crushed and pieces with the dimensions ~50 μm were selected for data collection. Single-crystal diffraction data were collected on a Rigaku Synergy R single-crystal diffractometer equipped with a rotating microfocus copper X-ray source, a Hypix 6000 detector and an Oxford Cryostream 800 plus low-temperature device. Data were collected at 180 K, with ~9000 frames recorded for each sample. Data reduction was done using the CrysAlisPro software.

Crystal structure analysis. The crystal structures of $Sr_4Nb_2O_9$ and $Sr_5Nb_2O_{10}$ were initially solved by a charge-flipping algorithm applied to the single crystal X-ray diffraction (SXRD) data using the software JANA2006[11] and the Superflip[12]. The solved structures were then refined by Rietveld refinements against Syn-PXRD and PND data to achieve the best accuracy. TOPAS Academic (TA)[13, 14] was employed during the Rietveld refinements. A small intensity weighting (5%) was applied to the Syn-PXRD data to schiece the most stable refinement. The occupancies of ions/sites were constrained to be consistent with the nominal compositions. All crystal structure visualization was done using the program VESTA [15].

Impedance analysis. The conductivities of sintered $Sr_4Nb_2O_9$ and $Sr_5Nb_2O_{10}$ pellets were measured using an MTZ-35 impedance analyzer (Bio-Logic). The samples were loaded into an HTSH-1100 high-temperature sample holder between two 13 mm diameter platinum plate electrodes (Bio-Logic) and measured from 100 ℃ to 800 ℃ with 50 ℃/step under high purity O_2 that had been dried by passing through condensed (98%) H_2SO_4 added with P_2O_5. The alternating (AC, 0.5 V) sweeping range selected was 0.1 to 1.0×10^6 Hz.

Results and Discussions

Structure of $Sr_4Nb_2O_9$ and $Sr_5Nb_2O_{10}$. The single-crystal X-ray diffraction data of $Sr_4Nb_2O_9$ and $Sr_5Nb_2O_{10}$ at 180 K were collected through a full reciprocal sphere with the resolution 0.8 Å to check the symmetry and space group. The observed reflections were well-indexed with the unit cell a = 8.275Å, b = 8.273 Å, c = 8.270 Å, α = 90.05º, β = 90.00º, γ = 89.99º, V = 566.1 Å^3 for $Sr_4Nb_2O_9$ and a = 8.292Å, b = 8.304 Å, c = 8.294 Å, α = 89.99º, β = 89.99º, γ = 90.05º, V = 571.1 Å^3 for $Sr_5Nb_2O_{10}$. Within the uncertainties of the SXRD analysis, the unit cells are cubic with a = 8.273 Å and 8.297 Å for $Sr_4Nb_2O_9$ and $Sr_5Nb_2O_{10}$, respectively. Images of reconstructed 3D Edward spheres projected along $[0\ 0\ 1]^*$, $[0\ 1\ 1]^*$, and $[1\ 1\ 1]^*$ are shown in Figure 1. Similar reflection behaviors are observed for $Sr_4Nb_2O_9$ and $Sr_5Nb_2O_{10}$, which agrees with the conclusion that they form a solid-solution.

After data reduction, two *F*-centred space groups were suggested: the $Fm\bar{3}m$ (225) one as reported in literature,[6] and a new $F\bar{4}3m$ (216) one. Referring to the $Fm\bar{3}m$ (225) structure model, Rietveld refinements were carried out against the SXRD data of $Sr_4Nb_2O_9$ and $Sr_5Nb_2O_{10}$ and fairly good agreements were achieved with weighted residual factors (R_{wp}) of 0.092 and 0.091, respectively. The crystal structure model with $F\bar{4}3m$ (216) was also constructed and refined against SXRD data. Slightly better agreements were then achieved with R_{wp} of 0.082 and 0.086, respectively. Further discussions concerning the differences between $Fm\bar{3}m$ (225) and $F\bar{4}3m$ (216) can be found in the following sections.

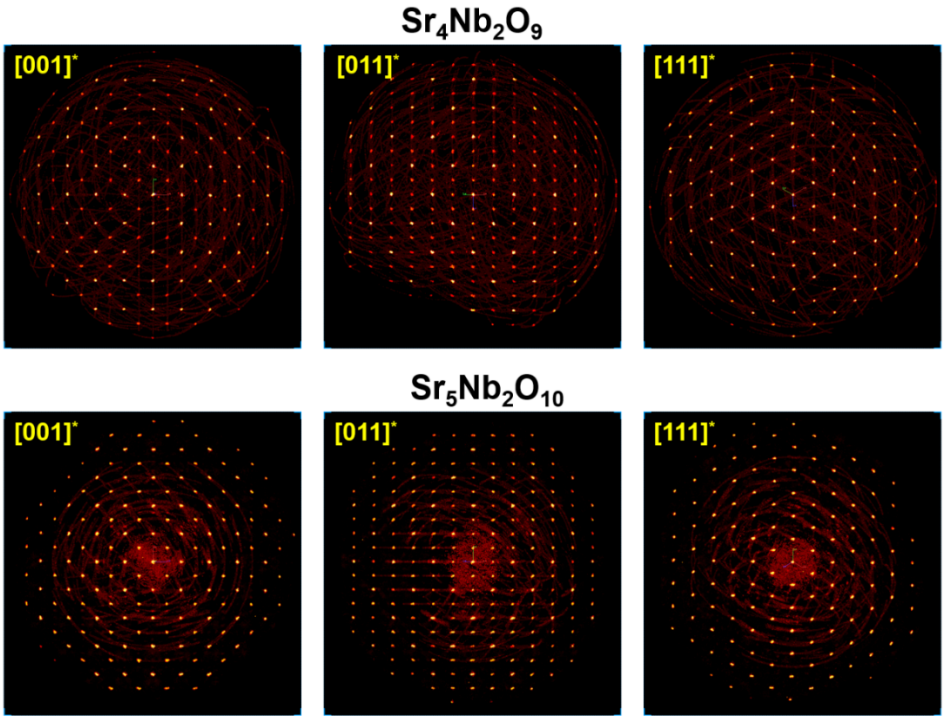

Figure 1. Images of reconstructed 3D SXRD Edward spheres projected along [0 0 1]*, [0 1 1]*, and [1 1 1]* for $Sr_4Nb_2O_9$ and $Sr_5Nb_2O_{10}$.

Powder neutron diffraction (PND) and synchrotron X-ray diffraction (Syn-PXRD) patterns of the $Sr_4Nb_2O_9$ and $Sr_5Nb_2O_{10}$ polycrystalline samples are shown in Figure 2. The combined refinements using the $Fm\bar{3}m$ (225) structure model reported by Li and Hong [6] were applied with the refined profiles showing in the figures. The weighted residual factors (R_{wp}) are 0.052 (overall), 0.045 (Syn-PXRD), 0.063 (PND) for $Sr_4Nb_2O_9$ and 0.035 (overall), 0.027 (Syn-PXRD), 0.050 (PND) for $Sr_5Nb_2O_{10}$, indicating good agreement with the diffraction data from the refinements using the $Fm\bar{3}m$ model. The square-root intensity is shown for Syn-PXRD data to highlight the weak reflections. All the observed reflections agree well with the lattice predictions in *d*-spacing, especially in the Syn-PXRD patterns, indicating that any impurities must be at a level <<1 wt.%. Details of the

refined structures are shown in Table 1 and given in the crystallographic information files (CIF) in supporting information (SI). Parameters of unit cells from our refinements agree with those reported by Li and Hong[6], e.g., the cell constant *a* of $Sr_4Nb_2O_9$ given as 8.2690(1) Å[6] was refined as 8.26832(1) Å here and that of $Sr_5Nb_2O_{10}$ given as 8.3014(1) Å[6] was refined as 8.30399(2) Å in this work. The higher precision obtained in the present work reflects the high quality of the synchrotron X-ray data.

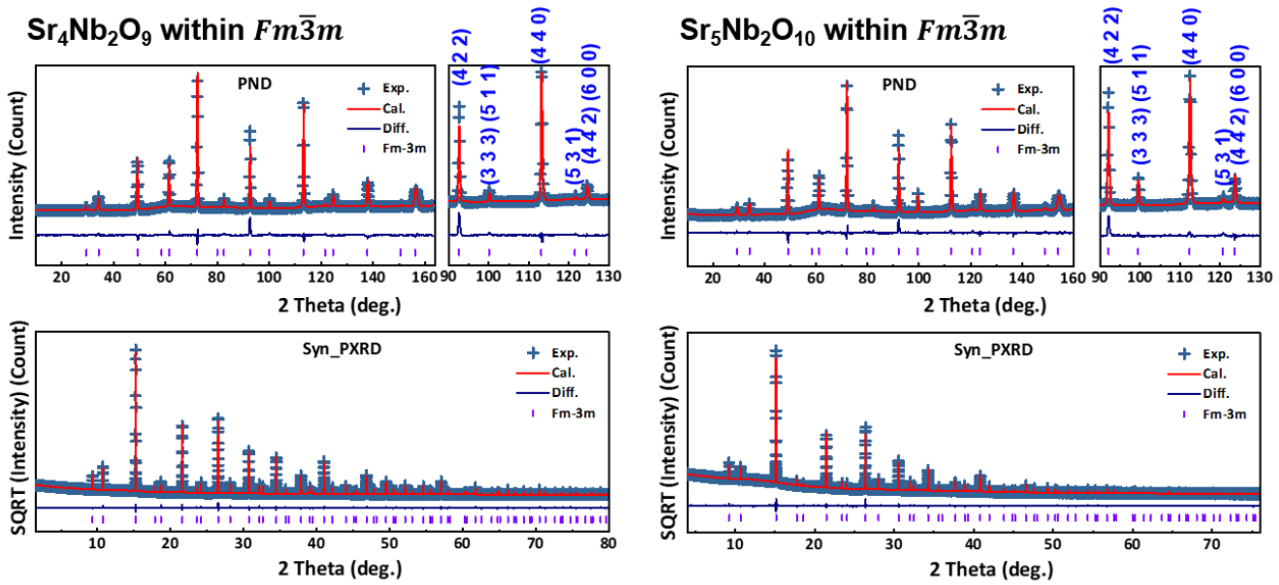

Figure 2. Rietveld-refined profiles of $Sr_4Nb_2O_9$ and $Sr_5Nb_2O_{10}$ within $Fm\bar{3}m$ (225) model. Top: PND (wavelength: 2.4395 Å), the whole 2θ range and zoomed 2θ range; bottom: syn-PXRD (wavelength: 0.774347 Å). Cross points, observed; solid line, calculated curve; solid line below the data is the difference curve; vertical tick marks, peak positions. Note: the intensity of syn-XRD data is plotted on a square-root scale to highlight the weak reflections.

For the powder diffraction data (PND and Syn-PXRD) collected, we also ran combined Rietveld refinements using the $F\bar{4}3m$ (216) model constructed from the SXRD analysis discussed above. The refined profiles are shown in Figure 3. Details of the refined structures are shown in Table 2 and given in the CIF files in the SI. The weighted residual factors (R_{wp}) are 0.045 (overall), 0.044 (Syn-PXRD), 0.046 (PND) for $Sr_4Nb_2O_9$ and 0.030 (overall), 0.026 (Syn-PXRD), 0.038 (PND) for $Sr_5Nb_2O_{10}$, indicating slightly better refinements using the $F\bar{4}3m$ (216) model than the $Fm\bar{3}m$ model, especially for the PND data. Selected regions of the PND patterns are shown in Figure 2 and Figure 3. The reflections of (4 2 2) and (5 3 1) are clearly underestimated by the $Fm\bar{3}m$ model but correctly described by the $F\bar{4}3m$ model.

Table 1. Structural parameters of $Sr_4Nb_2O_9$ and $Sr_5Nb_2O_{10}$ in the $Fm\bar{3}m$ (225) model from combined Rietveld refinements

against neutron and synchrotron X-ray powder diffraction data

Space Group	$Fm\bar{3}m$ (225)	
Formula	$Sr_4Nb_2O_9$	$Sr_5Nb_2O_{10}$
a (Å)	8.26832(1)	8.30398(2)
b (Å)	8.26832(1)	8.30398(2)
c (Å)	8.26832(1)	8.30398(2)
V (Å)	565.265(2)	572.611(3)
d_{theory} (g/cm^3)	5.303(1)	5.193(2)
R_{wp}	0.052 (overall), 0.045 (Syn-PXRD), 0.063 (PND), 0.092(SXRD)	0.035 (overall), 0.027 (Syn-PXRD), 0.050 (PND), 0.091(SXRD)

Atom	Site	Coordinate	Occupancy	B_{eq} (Å^2)	Coordinate	Occupancy	B_{eq} (Å^2)
Sr1	8*c* (1/4,1/4,1/4)		1	3.21(1)			5.53(3)
Nb1	4*a* (0,0,0)		1	1.02(1)			1.66(3)
Sr2	4*b* (1/2,1/2,1/2)		0.654(1)	4.34(2)		0.855(2)/	8.80(5)
Nb2			0.327(1)			0.142(1)	
O1	24*e* (x_1,0,0)	x_1 = 0.2401(2)	0.790(1)	4.40(2)	x_1 = 0.2417(2)	0.622(1)	4.26(3)
O2	48*h* (0, y_2, y_2)	y_2 = 0.1642(4)	0.102(1)	4.40(2)	y_2 = 0.1671(2)	0.165(1)	4.26(3)

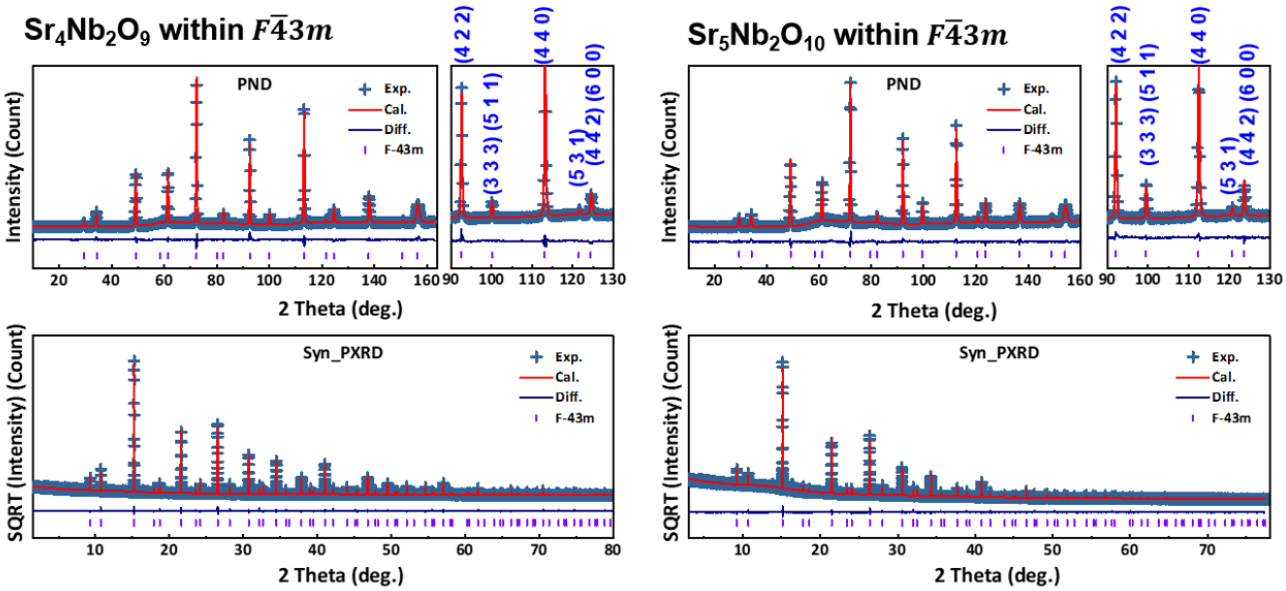

Figure 3. Rietveld-refined profiles of $Sr_4Nb_2O_9$ and $Sr_5Nb_2O_{10}$ using the $F\bar{4}3m$ (216) model. Top: PND (wavelength: 2.4395 Å), the whole 2θ range and zoomed 2θ range; bottom: syn-PXRD (wavelength: 0.774347 Å). Cross points, observed; solid line, calculated curve; solid line below the data is the difference curve; vertical tick marks, peak positions. Note: the intensity of syn-XRD data is plotted on a square-root scale to highlight the weak reflections.

Table 2. Structural parameters of $Sr_4Nb_2O_9$ and $Sr_5Nb_2O_{10}$ in the $F\bar{4}3m$ (216) model from combined Rietveld refinements against neutron and synchrotron X-ray powder diffraction data

Space Group	$F\bar{4}3m$ (216)	
Formula	$Sr_4Nb_2O_9$	$Sr_5Nb_2O_{10}$
a (Å)	8.268318(6)	8.303973(15)

b (Å)	8.268318(6)	8.303973(15)
c (Å)	8.268318(6)	8.303973(15)
V (Å)	565.2642(12)	572.609(3)
d_{theory} (g/cm^3)	5.308 (1)	5.180 (2)
R_{wp}	0.045 (overall), 0.044 (PXRD), 0.046 (PND), 0.082(SXRD)	0.030 (overall), 0.026 (PXRD), 0.038 (PND), 0.086(SXRD)

	Site	Coordinate	Occupancy	B_{eq} (Å^2)	Coordinate	Occupancy	B_{eq} (Å^2)
Sr1	4*c* (1/4, 1/4, 1/4)		1	2.80(4)		1	5.46(7)
Sr2	4*d* (3/4, 3/4, 3/4)		1	3.40(4)		1	5.67(8)
Nb1	4*a* (0,0,0)		1	1.04(1)		1	1.75(3)
Sr3 Nb2	4*b* (1/2, 1/2, 1/2)		0.656(1) 0.328(1)	4.17(2)		0.848(2) 0.139(1)	7.79(4)
O1	24*f* (x_1,0,0)	x_1= 0.2397(13)	0.344(2)	2.21(4)	x_1= 0.2479(6)	0.417(7)	1.78(5)
O2	48*h* (x_2, x_2, z_2)	x_2 = 0.1564(4) z_2= -0.006(2)	0.084(1)	2.21(4)	x_2 = 0.1657(3) z_2= -0.0125(13)	0.133(1)	1.78(5)
O3	48*h* (x_3, x_3, z_3)	x_3 = 0.5367(9) z_2 = 0.2423(11)	0.251(7)	2.21(4)	x_3= 0.5524(10) z_3= 0.2249(9)	0.134(4)	1.78(5)

$Fm\bar{3}m$ model versus $F\bar{4}3m$ model. The crystal structures of $Sr_4Nb_2O_9$ in the $Fm\bar{3}m$ and $F\bar{4}3m$ models are shown in Figure 4. Crystal structure models of $Sr_5Nb_2O_{10}$ are similar to those of $Sr_4Nb_2O_9$. The cation arrangement and coordination polyhedra in the two models are quite similar. Space group $F\bar{4}3m$ (216) is a maximal non-isomorphic subgroups of $Fm\bar{3}m$ (225). The relationships between Wyckoff positions in $F\bar{4}3m$ (216) and $Fm\bar{3}m$ (225) are listed in Table 3. The cations (Sr^{2+}, Nb^{5+}) and O1 in the $F\bar{4}3m$ model are mathematically correlated with those of the $Fm\bar{3}m$ model. The interstitial O2 at 48*h* in $F\bar{4}3m$ (216) slightly deviates from O2 at 48*h* in $Fm\bar{3}m$ (225). Moreover, an interstitial O3 at 48*h* in $F\bar{4}3m$ (216) is observed, which is near the O1 site. We also tried Rietveld refinements using the $Fm\bar{3}m$ model with an extra O3 site and found no significant improvements to the refinements. Thus, the subgroup $F\bar{4}3m$ (216) is critical to accommodate the new interstitial O^{2-}. Nb1 and its O^{2-} coordination polyhedra in $Sr_4Nb_2O_9$ for both models are shown in Figure 5 to show the difference between them. The symmetries are O_h and T_d, respectively. The O1 site in $Fm\bar{3}m$ splits into an O1 and two O3 in $F\bar{4}3m$, suggesting a freezing of the vibration/rotation of Nb−O octahedra/polyhedra to give an average ionic "cloud". This should be favourable for oxide ionic conductivity/migration. The distances between nearest-neighbour O3 ions is 0.86(2) Å in $Sr_4Nb_2O_9$ and 1.23(2) Å in $Sr_5Nb_2O_{10}$, i.e., O1−O3 spreads over a larger range in $Sr_5Nb_2O_{10}$ than in $Sr_4Nb_2O_9$.

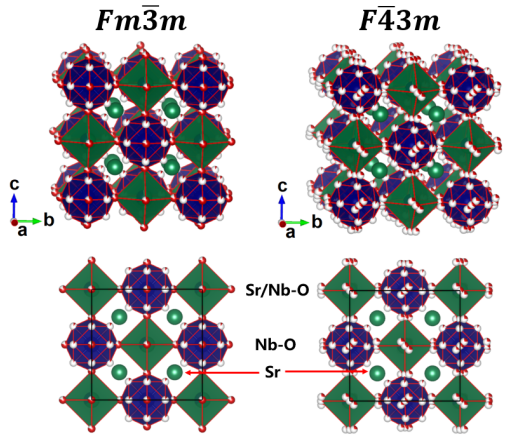

Figure 4. Crystal structure of $Sr_4Nb_2O_9$ in $Fm\bar{3}m$ and $F\bar{4}3m$ models. Sr2/Nb2−O1 octahedra in the $Fm\bar{3}m$ model and Sr3/Nb2−O1 octahedra in the $F\bar{4}3m$ model are green and Nb−O polyhedra are blue. Red = O^{2-}, small green = Sr^{2+}, blue = Nb^{5+}. The partial coloring of balls indicates mixed/partial occupancy.

Table 3. Correlation of Wyckoff positions in the $F\bar{4}3m$ (216) and $Fm\bar{3}m$ (225) models.

$F\bar{4}3m$ (216)		$Fm\bar{3}m$ (225)	
Sr1	4*c*	Sr1	8*c*
Sr2	4*d*		
Nb1	4*a*	Nb1	4*a*
Sr3/Nb2	4*b*	Sr2/Nb2	4*b*
O1	24*f*	O1	24*e*
O2	48*h*	O2[(a)]	48*h*
O3	48*h*	--	--

[(a)] The O2 at 48*h* in $F\bar{4}3m$ (216) is approximately correlated to O2 at 48*h* in $Fm\bar{3}m$ (225).

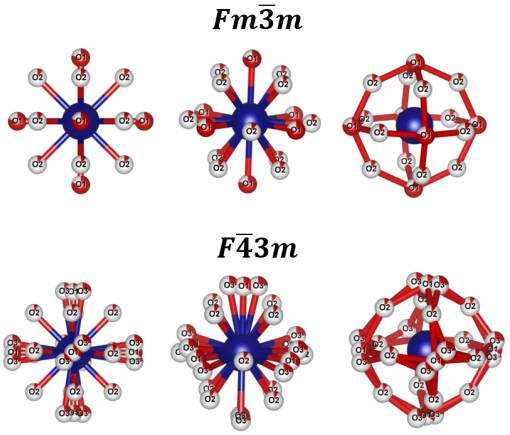

Figure 5. Local coordination of Nb−O in $Sr_4Nb_2O_9$ within the $Fm\bar{3}m$ and $F\bar{4}3m$ models. The partial coloring of balls indicates partial occupancy.

Conductivity of $Sr_4Nb_2O_9$ and $Sr_5Nb_2O_{10}$. The temperature-dependent conductivities of $Sr_4Nb_2O_9$ and $Sr_5Nb_2O_{10}$ ceramics in dried O_2 were studied using impedance spectroscopy. The conductivity was estimated by equivalent-circuit fitting of the impedance data at different temperatures using a parallel resistor (R) and constant phase

element (CPE), as plotted in Figure 6. The conductivities measured here are generally smaller than reported by Li and Hong[6] (e.g., for $Sr_5Nb_2O_{10}$ at 800 °C, in this work 2.2×10^{-5} S/cm versus 1.1×10^{-3} S/cm reported). This is due to the drier atmosphere used here [high-purity gas dried by passing through condensed (98%) H_2SO_4 added with P_2O_5]. The conductivity of $Sr_5Nb_2O_{10}$ is higher than that of $Sr_4Nb_2O_9$ (e.g., 2.2×10^{-5} S/cm versus 5.3×10^{-5} S/cm at 800 °C). In light of the distance (range) of O3 in the crystal structure as discussed above, the crystallographic arrangement (spreading) of O1 and O3 is likely to be play key structural role in oxide ionic migration. We are planning further dynamics studies in the future. The activation energies of $Sr_4Nb_2O_9$ and $Sr_5Nb_2O_{10}$ were estimated as 1.18(1) eV and 1.17(4) eV respectively from Arrhenius plots of the bulk conductivity (σ).

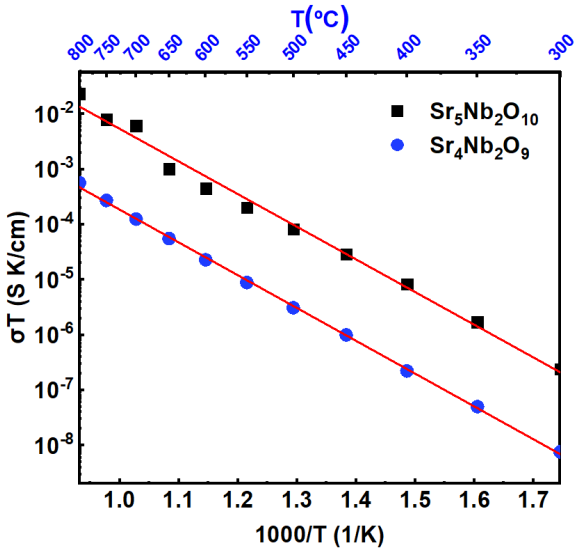

Figure 6. Temperature-dependent conductivities of $Sr_4Nb_2O_9$ and $Sr_5Nb_2O_{10}$ in dried O_2.

Conclusion

Polycrystalline and single-crystal $Sr_4Nb_2O_9$ and $Sr_5Nb_2O_{10}$ samples in the high-temperature cubic phase were synthesized. The crystal structures of $Sr_4Nb_2O_9$ and $Sr_5Nb_2O_{10}$ were studied using single crystal X-ray diffraction (SXRD), synchrotron powder X-ray diffraction (Syn-PXRD) and powder neutron diffraction (PND) data. In place of the previously reported $Fm\bar{3}m$ (225) model, we propose a new model in the subgroup $F\bar{4}3m$ (216), which gives a better fit to PND data. This new model contains an interstitial O3 at 48*h*, close to the O1 site, resulting in tetrahedral (T_d) coordination of Nb1-O rather than the octahedral (O_h) coordination found in the $Fm\bar{3}m$ (225) model. The temperature-dependent conductivities of $Sr_4Nb_2O_9$ and $Sr_5Nb_2O_{10}$ in dried O_2 were studied using impedance spectroscopy. The activation energies of $Sr_4Nb_2O_9$ and $Sr_5Nb_2O_{10}$ were estimated

to be 1.18(1) eV and 1.17(4) eV respectively from Arrhenius plots of the bulk conductivity (σ). The crystallographic arrangement of O1 and O3 (spread over two split sites) is likely to be a key structural factor behind oxide ionic migration in $Sr_4Nb_2O_9$ and $Sr_5Nb_2O_{10}$.

Acknowledgements

This work was supported by the National Natural Science Foundation of China (22075229), Natural Science Foundation of Shaanxi Province (2020JM-117), Fundamental Research Funds for the Central Universities, China, and the Australian Research Council – Discovery Projects scheme (CHW, BJK, CDL). This research was undertaken, in part, on the Powder Diffraction beamline at the Australian Synchrotron and the ECHIDNA beamline at the Australian Centre for Neutron Scattering (ACNS), both operated by the Australian Nuclear Science and Technology Organisation (ANSTO).

Reference

1. N. Mahato, A. Banerjee, A. Gupta, S. Omar and K. Balani, "Progress in material selection for solid oxide fuel cell technology: A review", *Prog. Mater. Sci.* **72**, 141-337 (2015).
2. W. H. Kan, A. J. Samson and V. Thangadurai, "Trends in electrode development for next generation solid oxide fuel cells", *J. Mater. Chem. A* **4** (46), 17913-17932 (2016).
3. S. J. Skinner and J. A. Kilner, "Oxygen ionic conductors", *Materials Today*, 30-37 (2003).
4. T. H. Etsell and S. N. Flengas, "Electrical properties of solid oxide electrolytes", *Chem. Rev.* **70** (3), 339-376 (1970).
5. V. Kharton, F. Marques and A. Atkinson, "Transport properties of solid oxide electrolyte ceramics: a brief review", *Solid State Ionics* **174** (1-4), 135-149 (2004).
6. M.-R. Li and S.-T. Hong, "Interstitial oxygen in perovskite-related $Sr_{6-2x}Nb_{2+2x}O_{11+3x}$", *Chem. Mater.* **20** (8), 2736-2741 (2008).
7. J. Y. Chan, I. Levin, T. A. Vanderah, R. G. Geyer and R. S. Roth, "Subsolidus phase relations and dielectric properties in the SrO-Al_2O_3-Nb_2O_5 system", *Int. J. Inorg. Mater.* **2** (1), 107-114 (2000).
8. I. Levin, J. Y. Chan, J. H. Scott, L. Farber, T. A. Vanderah and J. E. Maslar, "Complex polymorphic behavior and dielectric properties of perovskite-related $Sr(Sr_{1/3}Nb_{2/3})O_3$", *J. Solid State Chem.* **166** (1), 24-41 (2002).
9. M. Avdeev and J. R. Hester, "ECHIDNA: a decade of high-resolution neutron powder diffraction at OPAL", *Journal of Applied Crystallography* **51** (6), 1597-1604 (2018).
10. K. S. Wallwork, B. J. Kennedy and D. Wang, "The High Resolution Powder Diffraction Beamline for the Australian Synchrotron", **879** (1), 879-882 (2007).
11. V. Petricek, M. Dusek and L. Palatinus, "Crystallographic Computing System JANA2006: General features", *Z. Kristallogr.* **229** (5), 345-352 (2014).
12. L. Palatinus, "Ab initio determination of incommensurately modulated structures by charge flipping in superspace", *Acta Crystallogr. A* **60**, 604-610 (2004).
13. A. A. Coelho, J. S. O. Evans, I. R. Evans, A. Kern and S. Parsons, "The TOPAS symbolic computation system", *Powder Diffr.* **26**, S22-S25 (2011).

14. J. S. O. Evans, in "Extending the Reach of Powder Diffraction Modelling by User Defined Macros", edited by P. Scardi and R. E. Dinnebier (2010), Vol. 651, pp. 1-9.
15. K. Momma and F. Izumi, "VESTA 3 for three-dimensional visualization of crystal, volumetric and morphology data", *J. Appl. Crystallogr.* **44**, 1272-1276 (2011).